Eddy Lifetime, Number, and Diffusivity and the Suppression of Eddy Kinetic Energy in Midwinter

SEBASTIAN SCHEMM

Geophysical Institute, and Bjerknes Centre for Climate Research, University of Bergen, Bergen, Norway, and Institute for Atmospheric and Climate Science, ETH Zürich, Zurich, Switzerland

TAPIO SCHNEIDER

California Institute of Technology, Pasadena, California

(Manuscript received 26 September 2017, in final form 10 April 2018)

ABSTRACT

The wintertime evolution of the North Pacific storm track appears to challenge classical theories of baroclinic instability, which predict deeper extratropical cyclones when baroclinicity is highest. Although the surface baroclinicity peaks during midwinter, and the jet is strongest, eddy kinetic energy (EKE) and baroclinic conversion rates have a midwinter minimum over the North Pacific. This study investigates how the reduction in EKE translates into a reduction in eddy potential vorticity (PV) and heat fluxes via changes in eddy diffusivity. Additionally, it augments previous observations of the midwinter storm-track evolution in both hemispheres using climatologies of tracked surface cyclones. In the North Pacific, the number of surface cyclones is highest during midwinter, while the mean EKE per cyclone and the eddy lifetime are reduced. The midwinter reduction in upper-level eddy activity hence is not associated with a reduction in surface cyclone numbers. North Pacific eddy diffusivities exhibit a midwinter reduction at upper levels, where the Lagrangian decorrelation time is shortest (consistent with reduced eddy lifetimes) and the meridional parcel velocity variance is reduced (consistent with reduced EKE). The resulting midwinter reduction in North Pacific eddy diffusivities translates into an eddy PV flux suppression. In contrast, in the North Atlantic, a milder reduction in the decorrelation time is offset by a maximum in velocity variance, preventing a midwinter diffusivity minimum. The results suggest that a focus on causes of the wintertime evolution of Lagrangian decorrelation times and parcel velocity variance will be fruitful for understanding causes of seasonal storm-track variations.

1. Introduction

Extratropical cyclones control weather variability. They preferentially occur in regions that are commonly referred to as storm tracks. Near the storm-track entrances, equator–pole temperature gradients are strongest and baroclinic instability drives the release of available potential energy. Many properties of storm tracks are controlled by processes affecting the equator–pole temperature gradients and the static stability of the atmosphere (e.g., Fyfe 2003; Yin 2005; Bengtsson et al. 2006; Schneider and Walker 2008; O'Gorman and Schneider 2008; O'Gorman 2010; Harvey et al. 2014). Consequently, the future development of midlatitude equator–pole temperature gradients and static stability is a key to understanding future storm-track behavior, with the relative importance of various processes still under debate [see Chang et al. (2002), Schneider et al. (2010), and Shaw et al. (2016) for reviews].

Baroclinic instability is widely accepted as the formation mechanism of extratropical cyclones, and baroclinicity, which is proportional to the meridional temperature gradient and inversely proportional to static stability, quantifies their growth potential (Charney 1947; Eady 1949; Lindzen and Farrell 1980). As noted by classical theory and supported by observations, higher baroclinicity usually leads to deeper and

Denotes content that is immediately available upon publication as open access.

Corresponding author: Sebastian Schemm, sebastian.schemm@uib.no

DOI: 10.1175/JCLI-D-17-0644.1

© 2018 American Meteorological Society. For information regarding reuse of this content and general copyright information, consult the AMS Copyright Policy (www.ametsoc.org/PUBSReuseLicenses).

more rapidly intensifying extratropical cyclones. Because extratropical cyclone activity is intimately linked to poleward heat transport, increased baroclinicity generally also implies intensified poleward eddy heat flux (e.g., Schneider and Walker 2008; Thompson and Birner 2012). Observational studies suggest that variations in the equator-to-pole temperature contrast often dominate baroclinicity variations (Ambaum and Novak 2014; Thompson and Barnes 2014). In fact, Stone and Miller (1980) found that seasonal variations of the meridional eddy energy flux show an excellent correlation with variations in the meridional surface temperature gradient.

However, the midwinter evolution of the North Pacific storm track appears to challenge these classical theories and observations (Nakamura 1992). Although the surface temperature gradient peaks during midwinter, several measures of eddy activity, such as the meridional eddy energy flux and the transient eddy kinetic energy (EKE), have a minimum in midwinter over the North Pacific (Nakamura 1992). Several mechanisms explaining this phenomenon have been proposed:

- The increased group velocity of eddies in winter can result in wave packets passing too quickly through the main baroclinic zone, causing a suppression of their baroclinic amplification (Chang 2001).
- The narrow jet stream in midwinter (Harnik and Chang 2004), the jet's more subtropical nature and a related meridional displacement of the lower- and upper-baroclinic zone (Nakamura and Sampe 2002), or the enhanced barotropic deformation of eddies (Deng and Mak 2005) may contribute to suppression of eddy growth.
- A reduced frequency of upper-tropospheric cyclogenesis over midlatitude Asia, upstream of the North Pacific storm track, may lead to the midwinter suppression of eddy activity (Penny et al. 2010). Additionally, the central Asian mountains affect stationary waves that disorganize wave packets more strongly during midwinter compared to the shoulder seasons (Park et al. 2010). However, the role of upstream processes in the midwinter suppression of eddy activity has been questioned (Chang and Guo 2011; Penny et al. 2011; Chang and Guo 2012).
- Diabatic processes have been suggested to be important for the midwinter suppression of eddy activity, based on difficulties in producing a midwinter suppression in dry idealized models (Chang and Zurita-Gotor 2007). Chang (2001) found that diabatic heating generates eddy available potential energy during spring and fall, but acts to dissipate eddy kinetic energy during midwinter, in contrast to the situation over the North Atlantic (Chang 2001; Chang and Song 2006).

It is important to note that a mild midwinter plateau in transient EKE is also observed in the North Atlantic (see section 3). Therefore, it seems unlikely that any one of the aforementioned mechanisms alone, in particular if unique to the North Pacific, is sufficient to explain the observed seasonal storm-track variability.

To better understand how the midwinter suppression of EKE over the North Pacific translates into a midwinter suppression in eddy fluxes, we here provide Lagrangian diagnostics of eddy activity and connect them with Eulerian statistics, on the basis of the semiempirical flux–gradient relationship

$$\overline{v'T'} = -D\frac{\partial \overline{T}}{\partial y}. \tag{1}$$

Here, $\overline{v'T'}$ is the 800-hPa transient eddy heat flux, $\partial\overline{T}/\partial y$ is the meridional temperature gradient, and D is the empirical eddy diffusivity connecting the two. During midwinter over the North Pacific, the 800-hPa meridional temperature gradient is maximal (see Fig. 10). It follows that the eddy diffusivity must be responsible for any midwinter minimum in the lower-level eddy heat flux evolution. Because the eddy diffusivity can be represented as $D \approx \mathrm{EKE} \times \tau$, where τ is the Lagrangian decorrelation time (e.g., Swanson and Pierrehumbert 1997), changes in the eddy diffusivity can arise from the midwinter minimum in EKE or from a midwinter minimum in the Lagrangian decorrelation time τ, or from a combination of the two. The upper-level analogy to the lower-level heat flux in Eq. (1) is the meridional eddy potential vorticity (PV) flux, which we similarly analyze on the 320-K isentropic surface.

In this study, we determine the seasonal cycle of the relevant Eulerian and Lagrangian quantities entering the empirical eddy diffusivity over the North Pacific and compare it with the North Atlantic, in an attempt to shed light on mechanisms for the midwinter suppression of eddy activity. Further, we quantify the seasonal cycle of mean EKE per eddy life cycle, eddy number, and eddy lifetime, in order to understand the role of dynamics internal to storm tracks compared with the role of upstream seeding effects. These analyses are augmented and reinforced by an analysis of the seasonal cycle of baroclinic and barotropic conversion rates in the North Pacific and North Atlantic.

The paper is organized as follows: Section 2 introduces data and methods; section 3 presents the monthly variability of eddy characteristics inferred from

reanalysis data using objective cyclone tracking; section 4 quantifies the Lagrangian decorrelation time and estimates the eddy diffusivity by calculating particle trajectories over a period of 30 yr; and section 5 summarizes the conclusions.

2. Data and methods

All computations are based on 6-hourly ERA-Interim data for 1981–2010 (Dee et al. 2011), interpolated to a $1° \times 1°$ regular grid and 11 vertical pressure levels between 1000 and 100 hPa.

a. Frequency filtering

For the decomposition of the flow field into eddy and mean components, we use a Lanczos filter with 21 weights, which operates on the entire time series plus two boundary months that are removed after the computation. We start with the common 2–6-day bandpass filtering. Later, when computing the individual EKE forcing mechanisms, we decompose the flow into a high-frequency and low-frequency component with a 6-day cutoff so that the sum of both equals the full flow field. This avoids the computation of additional ambiguous transfer terms in the EKE tendency equation.

b. Cyclone detection

Cyclones are detected using a feature-based surface cyclone detection scheme that tracks closed isobars around a sea level pressure minimum based on 6-hourly unfiltered mean sea level pressure data on a $1° \times 1°$ regular grid. In this study, we make use of the Wernli and Schwierz (2006) algorithm [for a recent update of the algorithm, see the method section in Sprenger et al. (2017)]. Cyclone tracks are accepted if they live longer than 24 h. The contour search is performed in intervals of 0.5 hPa. All grid points inside the outermost closed contour are flagged with 1 and all grid points outside are flagged with 0, to obtain a cyclone mask. The cyclone detection rates are then expressed in terms of a frequency that indicates the percentage of time steps affected by a surface cyclone relative to all time steps. The frequency is computed by time averaging over all cyclone masks. The scheme does not identify anticyclones. For a detailed comparison of the algorithm's performance relative to other methods we refer to Neu et al. (2013).

c. Parcel trajectory computation

To estimate the eddy diffusivity, we compute Lagrangian trajectories of particles released every 12 h between 1981 and 2010 in the North Pacific and North Atlantic. The starting positions are at equidistant steps of 200 km in the horizontal, and at different pressure levels (800, 300, 250, and 200 hPa) in the vertical. The starting areas lie in the central North Pacific (20°–60°N, 170°E–170°W) and the central North Atlantic (20°–60°N, 20°–50°W,). Particle trajectories are computed using the Lagrangian analyses tool (LAGRANTO; Wernli and Davies 1997; Sprenger and Wernli 2015). The 30-yr climatology comprises approximately 3 000 000 trajectories per month.

To highlight regions with high particle density, a parcel probability density is computed. This is done as described in Schemm et al. (2016): First, all grid points within a radius of 300 km around the interpolated parcel position are flagged with a value of 1 to indicate the presence of a Lagrangian particle. The summed field is normalized by the gridpoint area and the total number of trajectories, then by its integral over Earth's surface. This results in a parcel probability density that evolves in time and integrates to unity at each time step after the parcel start.

d. EKE tendency

EKE forcing terms are computed following Orlanski and Katzfey (1991) and Orlanski and Sheldon (1995). Using the notation in Rivière et al. (2015), we derive the EKE tendency equation by multiplying the high-pass-filtered horizontal momentum equation in isobaric coordinates with the filtered horizontal velocity $\mathbf{u}'$. Representing viscous forces by $\mathbf{F}$, this leads to

$$\frac{\partial}{\partial t}\mathrm{EKE} = -\mathbf{u}' \cdot (\mathbf{u}_3 \cdot \nabla_3 \mathbf{u})' - \mathbf{u}' \cdot \nabla\phi' + \mathbf{u}' \cdot \mathbf{F}', \quad (2)$$

where $\mathrm{EKE} = 0.5\mathbf{u}'^2$, ϕ' is the filtered geopotential, and the subscript 3 denotes three-dimensional velocities and derivative operators. The first term on the right-hand side can be expressed as

$$-\mathbf{u}' \cdot (\mathbf{u}_3 \cdot \nabla_3 \mathbf{u})' = -\overline{\mathbf{u}}_3 \cdot \nabla_3 \mathrm{EKE} - \mathbf{u}_3' \cdot \nabla_3 \mathrm{EKE} - \mathbf{u}' \cdot (\mathbf{u}_3' \cdot \nabla_3 \overline{\mathbf{u}}) + R, \quad (3)$$

with the residual

$$R = -\mathbf{u}' \cdot (\overline{\mathbf{u}}_3 \cdot \nabla_3 \overline{\mathbf{u}}) + \mathbf{u}' \cdot \overline{(\mathbf{u}_3 \cdot \nabla_3 \mathbf{u})}. \quad (4)$$

The physical interpretation of the first three terms on the right-hand side of Eq. (3) are (i) the advection of EKE by the mean flow, (ii) advection of EKE by eddies, and (iii) barotropic conversion from mean to eddy kinetic energy. Note that we use high-pass- and low-pass-filtered velocities (6-day cutoff) in the definition of $\mathbf{u}'$

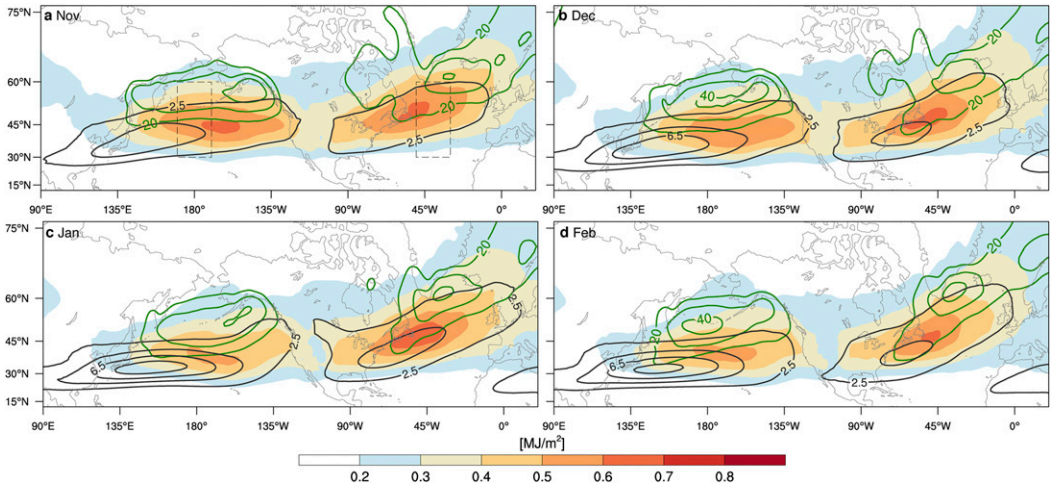

FIG. 1. Vertically integrated (1000–100 hPa) bandpass-filtered (2–6 day) EKE (color shading; MJ m^{-2}), time-mean KE (black contours at 2.5, 4.5, 6.5, and 8.5 MJ m^{-2}), and surface cyclone frequency (green contours at 20%, 30%, and 40%) during (a) November, (b) December, (c) January, and (d) February. Dashed black boxes in (a) indicate analysis regions for the Eulerian statistics in section 3.

and $\overline{\mathbf{u}}$, so that their sum equals the total horizontal flow field. Using bandpass-filtered velocities would result in additional transfer terms in Eq. (3) between different frequency bands. The residual terms collected in R are typically small and are not considered further.

Next, the pressure work term, the second term on the right-hand side of Eq. (2), is written with the continuity equation as

$$-\mathbf{u}' \cdot \nabla\phi' = \omega' \frac{\partial \phi'}{\partial p} - \nabla(\phi' \mathbf{u}'_a) - \frac{\partial}{\partial p}(\omega'\phi'), \qquad (5)$$

where the first term on the right-hand side is the baroclinic conversion, and the second and third terms are the horizontal and vertical convergence of the ageostrophic geopotential flux, with the subscript a denoting the ageostrophic horizontal velocity. In essence, the only true source terms are the baroclinic and barotropic conversion rates, while the flux divergences are redistributing EKE in the interior of the flow.

3. Observations

a. *Seasonal cycle of EKE, cyclone frequency, and jet stream position*

The North Pacific and North Atlantic storm tracks develop differently during the winter season. Over the central North Atlantic, vertically integrated (1000–100 hPa) EKE, computed based on 2–6-day bandpass-filtered wind

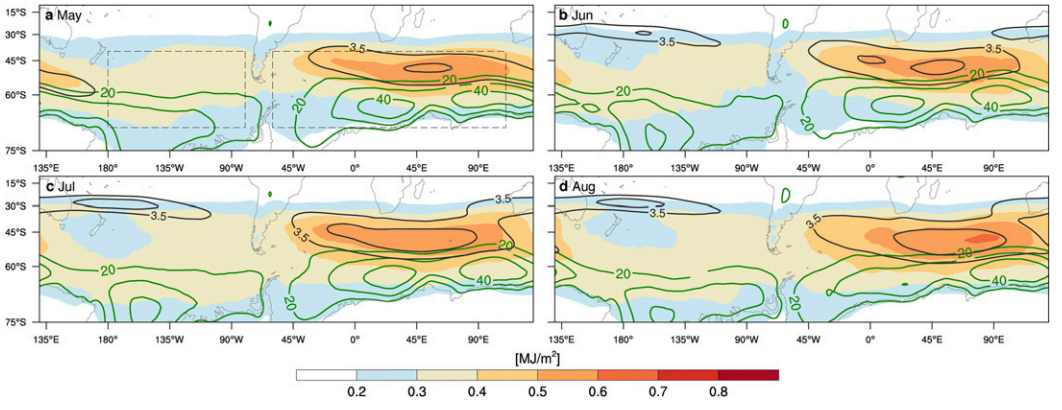

FIG. 2. Vertically integrated (1000–100 hPa) bandpass-filtered (2–6 day) EKE (color shading; MJ m^{-2}), KE (black contours at 3.5 and 4.5 MJ m^{-2}), and surface cyclone frequency (green contours at 20%, 30%, and 40%) during (a) May, (b) June, (c) July, and (d) August. Dashed black boxes in (a) indicate analysis regions for the Eulerian statistics in section 3.

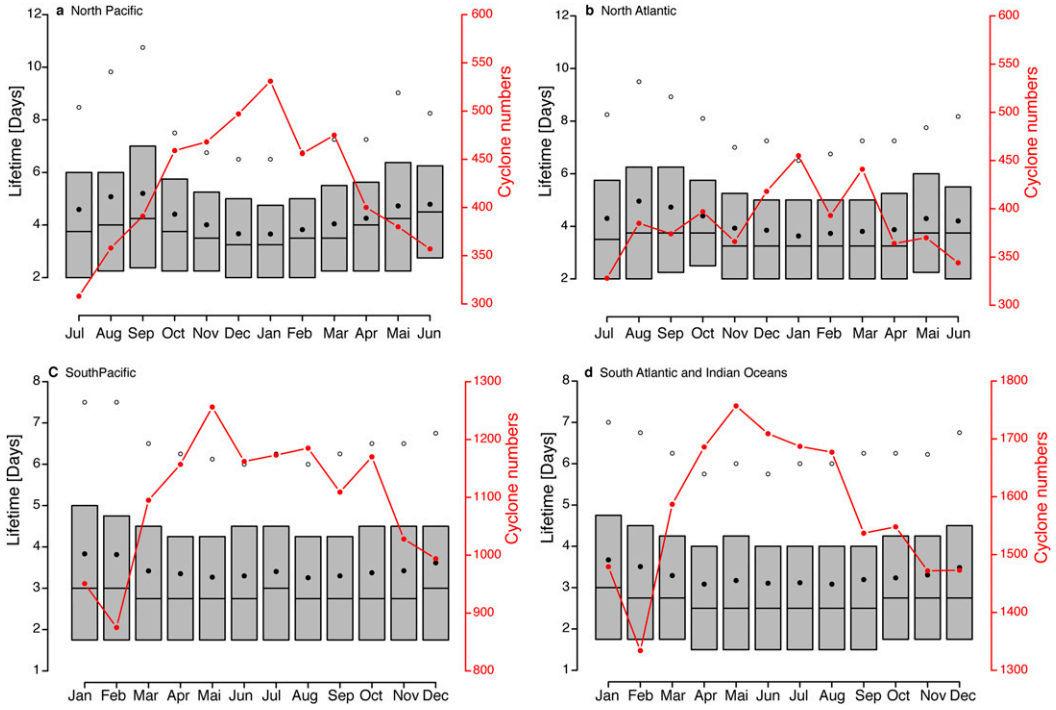

FIG. 3. Seasonal cycle of eddy lifetime and numbers (red curves). The box-and-whisker plots indicate the monthly lifetime distribution based on all surface cyclones that propagate through (a) the North Pacific (30°–60°N, 170°E–170°W), (b) the North Atlantic (30°–60°N, 30°–50°W), (c) the South Pacific (40°–70°S, 180°–80°W), and (d) the South Atlantic–Indian Oceans (40°–70°S, 60°W–110°E). Each gray-shaded box spans the interquartile range (25th–75th percentile), with the black line indicating the median and the black dots indicating the mean of the monthly lifetimes. Circles indicate the 90th percentile. The red curve indicates the number of cyclones per month between 1981 and 2010. The target areas are shown in Figs. 1a and 2a (dashed black boxes). After normalizing with the days per month, the relative minimum during February in the North Pacific vanishes (see text for cyclone numbers per day), while February and March have almost equal numbers in the North Atlantic.

fields, is highest during January; over the North Pacific, EKE is lower during January and highest during November (Fig. 1). The decline of EKE over the North Pacific starts after November (Fig. 1b), and EKE values greater than 5 MJ m^{-2} (red shading) are concentrated during January in a narrow region over the central North Pacific. In contrast, EKE in the North Atlantic increases from November to January and starts to decline afterward.

Maximum surface cyclone frequencies are concentrated toward the end of the North Pacific storm track and are shifted poleward relative to the maximum in EKE (Fig. 1, green contours). The former is a consequence of the reduced propagation speed of cyclones near the end of their life cycle. The poleward shift of the high cyclone frequencies relative to the maximum in EKE is to some extent the result of the typical poleward motion of eddies (e.g., Wallace et al. 1988; Baehr et al. 1999; Coronel et al. 2015). It potentially also relates to a higher propagation speed in regions of high cyclone intensity, reducing cyclone frequencies in regions of high intensity (similarly, lower cyclone frequencies are observed where the jet is strong and the propagation speed is high). Surface cyclone frequencies are only moderately changing between November and January (Figs. 1a–c). However, the maximum shifts into the central North Pacific during February (Fig. 1d). In the North Atlantic, there are two maxima in cyclone frequency. The first is located south of Greenland, a region where cyclones are known to merge, split, form, or decay, and a second maximum is located downstream north of Norway, at the end of the North Atlantic storm track. The overall structure of the surface storm tracks is in good agreement with cyclone-tracking statistics presented, for example, in Hoskins and Hodges (2002).

Vertically integrated mean kinetic energy (KE) depicts the mean position and strength of the upper-level jet (Fig. 1, black contours). In the North Pacific, the strongest jet is observed during January, which is shifted equatorward compared to its position during the shoulder seasons. The North Pacific jet is confined to a relatively

narrow range of latitudes. This is in contrast to the North Atlantic jet, which has a stronger southwest-to-northeast tilt. In both basins, maxima in EKE are displaced poleward relative to the jet's axis, in agreement with observations and quasigeostrophic (QG)-scaling arguments (e.g., Keyser and Shapiro 1986; Uccellini 1990).

In the Southern Hemisphere (SH), a split jet develops during midwinter (Fig. 2; Nakamura and Shimpo 2004). Cyclone frequencies are highest poleward of the EKE maxima, similar to the Northern Hemisphere (NH). Maximum EKE values above 6 MJ m^{-2} (dark red shading) are found during August (Fig. 2d). Compared to May, cyclone frequencies during midwinter are greater downstream and poleward of the EKE maximum and are smaller upstream (Figs. 2c,d, green contours). The SH appears not to be affected by a midwinter suppression of equal strength as is observed in the NH and is more persistent in location and strength (Trenberth 1991; Hoskins and Hodges 2005). However, maximum EKE values occur near the end of the winter season when the jet is also strongest (June–August).

b. *Seasonal cycle of eddy lifetime and eddy number*

Eddy lifetime is analyzed based on the automated cyclone detection. For eddies propagating through the central North Pacific (dashed black boxes in Fig. 1a) the lifetime decreases during midwinter, with lowest lifetimes identified during January (Fig. 3). The decrease of the mean lifetime is most pronounced in the North Pacific, which decreases from 5.2 days in September to 3.9 days in December. During spring, the lifetime increases again in both the North Atlantic and North Pacific (Figs. 3a,b). The interquartile range of lifetimes indicates reduced lifetime variability among the eddies during midwinter. The reduction of mean lifetime in midwinter arises primarily from a reduction in the frequency of long-lived eddies.

The number of surface cyclones increases through the winter and reaches a maximum in January, both in the North Pacific and the North Atlantic (Figs. 3a,b). For example, for the period 1981–2010, 531 cyclone tracks are identified in January[1] in the central North Pacific, and 455 are identified in the central North Atlantic (red curve in Figs. 3a,b). In the North Atlantic, the shoulder months of March and October experience a larger number of surface cyclones than in February and November, respectively, but the maximum is still reached during January (Fig. 3b). The relative minimum in cyclone numbers in the North Pacific during February is a result of the reduced number of days in February. The relative minimum is no longer observed after normalizing by the total number of days. In the North Atlantic, February and March have almost similar cyclone numbers per day. More specifically, in the North Pacific, the average cyclone number per day is 0.57 for January, 0.54 for February, and 0.51 for March. In the North Atlantic, the average cyclone number per day is 0.49 for January, 0.46 for February, and 0.47 for March.

The fact that most cyclones in the North Pacific storm track occur during winter, while their mean lifetime is shortest, seems to be in contrast with the conclusions of

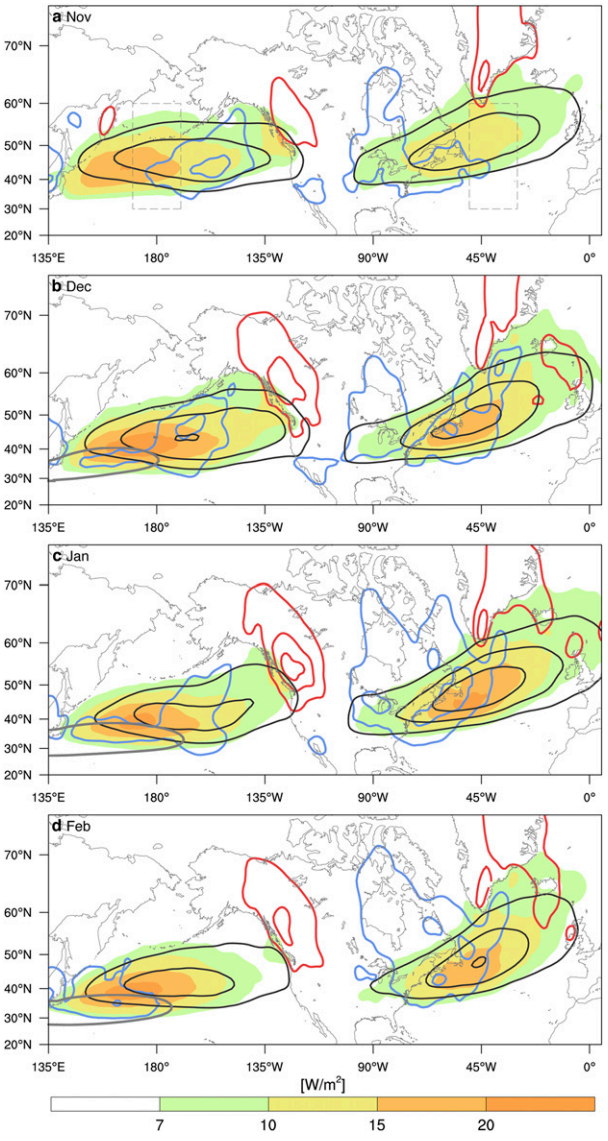

FIG. 4. Vertically integrated (1000–100 hPa) high-pass-filtered (6-day cutoff) EKE (black contours at 8, 10, and 12 MJ m^{-2}), baroclinic (color shading; W m^{-2}), and barotropic conversion (red contours positive and blue contours negative at 2.5, 5, and 7 W m^{-2}). Gray thin contours indicate vertically integrated KE in the Pacific of 65 MJ m^{-2}.

[1] Tracks that affect two months are not split, but categorized into one month according to the majority of time steps.

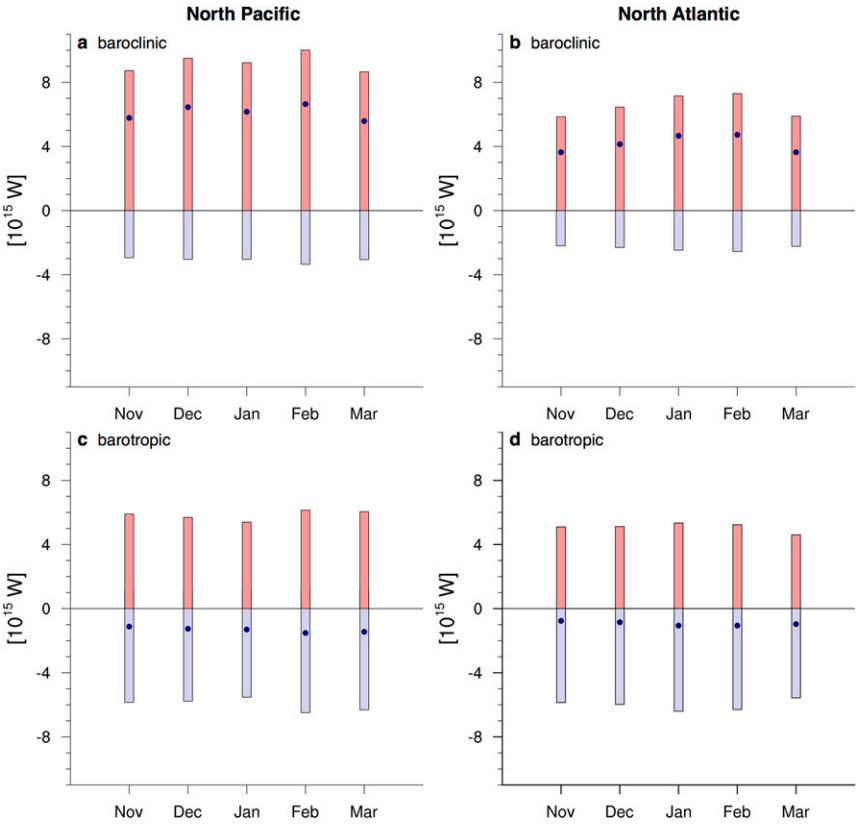

FIG. 5. Monthly mean volume–time-integrated (a),(b) baroclinic and (c),(d) barotropic EKE generation (red) and EKE destruction (blue). Baroclinic and barotropic conversion rates are volume integrated over the (left) North Pacific (25°–55°N, 145°E–145°W; 1000–100 hPa) and (right) North Atlantic (30°–60°N, 75°–55°W; 1000–100 hPa). Black dots indicate the monthly mean net contribution to EKE formation, which is positive for baroclinic conversion (i.e., acts as EKE source) and slightly negative for barotropic conversion (i.e., acts as EKE sink).

Penny et al. (2010). However, Penny et al. (2010) analyzed upper-level eddy activity at the 300-hPa level in spatially and temporally filtered geopotential height, while we identify surface cyclones in unfiltered mean sea level pressure. Therefore, the seasonal cycles of upper-level eddies (i.e., troughs and ridges) and surface cyclones may develop differently. Apparently, the reduced number of upper-levels eddies (Penny et al. 2010) still triggers more frequent surface cyclones during midwinter relative to the shoulder months. The fact that the mean lifetime is shortest is in agreement with the enhanced midwinter eddy propagation speed found by Chang (2001). In any case, our results do not support any general conclusion that the midwinter minimum over the Pacific would be caused by reduced surface cyclone numbers. Further, the midwinter reduction in upper-level eddy frequency apparently does not translate into a reduction in surface cyclone numbers.

The seasonal variability in eddy lifetime is less pronounced in the SH (Figs. 3c,d). But eddy numbers also peak during midwinter. In the Pacific sector of the Southern Ocean (40°–70°S, 180°–80°W; dashed light gray boxes in Fig. 2), the lifetime gradually decreases after the summer (December–February) and remains short during spring and winter (Fig. 3c). In the South Pacific, for the period of April–October, the eddy numbers fluctuate around 1100, with a maximum in May of approximately 1256 (red curve in Fig. 3). In the South Atlantic and Indian Ocean sector, the number of cyclones between April and August fluctuates around 1700, before it decreases to 1550 in October (Fig. 3d).

c. *Local EKE forcing, EKE per cyclone, and Lagrangian EKE tendency*

In the North Pacific, vertically integrated baroclinic conversion is larger during December than during January. Maximum baroclinic conversion occurs upstream of the maximum in EKE (Fig. 4a). More precisely, the area of high baroclinic EKE generation in the North

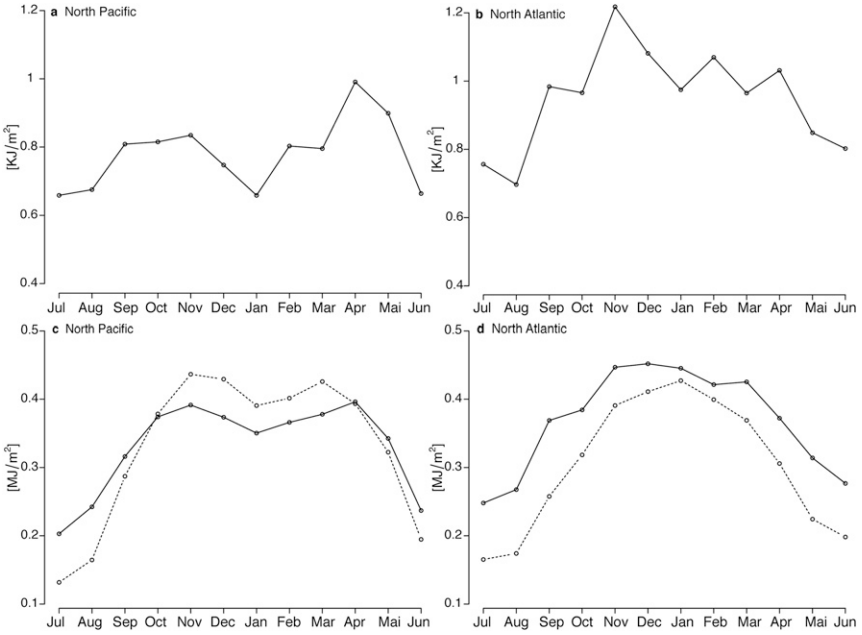

FIG. 6. Mean EKE per cyclone life cycle in the (a) central North Pacific and (b) central North Atlantic (kJ m^{-2}). Mean EKE per cyclone life cycle multiplied by number of cyclones in the (c) central North Pacific and (d) central North Atlantic (solid; MJ m^{-2}). Dashed lines indicate area-averaged EKE in the (c) central North Pacific and (d) central North Atlantic, computed from the monthly mean climatology shown in Fig. 1. EKE is vertically integrated (1000–100 hPa) and bandpass filtered (2–6 day). The target areas are shown in Fig. 1a (dashed black boxes).

Pacific grows from November to December and retreats and weakens during January. In contrast, baroclinic conversion peaks in the North Atlantic during January (Fig. 4c). However, because the baroclinic conversion from mean available potential energy to eddy available potential energy scales with the meridional eddy heat flux (Chang 2001), it is unclear if the midwinter minimum in baroclinic conversion is a cause or a consequence of the midwinter minimum in EKE and other measures of storm-track activity.

The barotropic conversion acts as an EKE sink along the core and exit of the climatological North Pacific jet, which is located upstream of the upper-level planetary pressure ridge in the winter climatology (Fig. 4, blue contours). Over the North Atlantic, the barotropic EKE sink is located near the North Atlantic jet entrance and collocated with the climatological upper-level pressure trough over the Gulf Stream. The North Pacific barotropic EKE sink follows closely the corresponding seasonal EKE cycle in both basins and hence is also affected by the midwinter suppression. Note that barotropic EKE generation occurs over western Canada under large-scale northeasterly flow conditions, downstream of the upper-level pressure ridge.

Is the suppression in baroclinic conversion (cf. Fig. 4) resulting from a suppression in baroclinic EKE generation or increase in baroclinic EKE destruction? To answer this, areas with positive EKE conversion and areas with negative EKE conversion rates are integrated separately every 6 h over time and volume,[2] encompassing the center of the North Pacific (25°–55°N, 145°E–145°W) and the North Atlantic storm tracks (30°–60°N, 75°–15°W). This allows us to quantify the monthly mean contribution of baroclinic and barotropic conversion rates to EKE tendencies (Fig. 5). Consistent with Fig. 4, the mean baroclinic growth rate is suppressed in the North Pacific during midwinter, albeit only mildly (Fig. 5a), while baroclinic EKE destruction does not exhibit a midwinter suppression. In contrast to baroclinic conversion rates, the barotropic conversion rates are small, and barotropic EKE generation and destruction both exhibit a midwinter suppression. In contrast to the North Pacific, baroclinic growth peaks in the North Atlantic during midwinter (Fig. 5b). But it remains unclear to what extent the suppression of barotropic and baroclinic conversion is a consequence or a cause of the EKE suppression, because the conversion into eddy available potential energy scales with the eddy heat flux.

[2] Mass-weighted in the vertical between 1000 and 100 hPa and area-integrated in the horizontal.

One of the questions arising from the reduction in mean EKE during midwinter is whether individual cyclones are weaker during the suppression. To answer this, we compute a mean EKE per cyclone life cycle by tracking vertically integrated EKE along every cyclone that propagates through the central North Pacific and North Atlantic. EKE is averaged inside a 1° × 1° box centered on the cyclone core. Afterward, the tracked EKE values are averaged over each track and over all tracks in one month. Dividing the obtained mean EKE by the number of cyclone tracks yields a mean EKE per cyclone life cycle. The resulting mean EKE per cyclone life cycle reveals a midwinter suppression in the North Pacific. The North Atlantic exhibits a midwinter plateau (Figs. 6a,b). When multiplied by the number of cyclone life cycles, the seasonal evolution of the mean EKE obtained from all cyclone tracks parallels that of the Eulerian-mean EKE (Figs. 6c,d). The discrepancy arises in parts from the chosen box size and potentially also because the Eulerian-mean EKE is resulting from the combined action of cyclones and anticyclones (the tracking scheme only identifies cyclones).

Next, we evaluate the Lagrangian EKE tendency along individual cyclone tracks by differencing EKE along subsequent time steps in a life cycle. During midwinter in the North Pacific, Lagrangian EKE tendencies are reduced relative to the shoulder months (Fig. 7a). This is not the case in the North Atlantic, where Lagrangian EKE tendencies peak during December–January (Fig. 7b).

To summarize, mean EKE per cyclone life cycle in the North Pacific is on average lower during January compared to the shoulder months. In the North Atlantic, mean EKE per cyclone life cycle is highest during December–January. As there is a larger number of surface cyclones propagating through the North Pacific during winter, plus a local reduction in baroclinic EKE growth and a reduction of mean EKE per cyclone life cycle, the North Pacific suppression appears to be more a consequence of local storm-track dynamics than a result of upstream seeding variability.

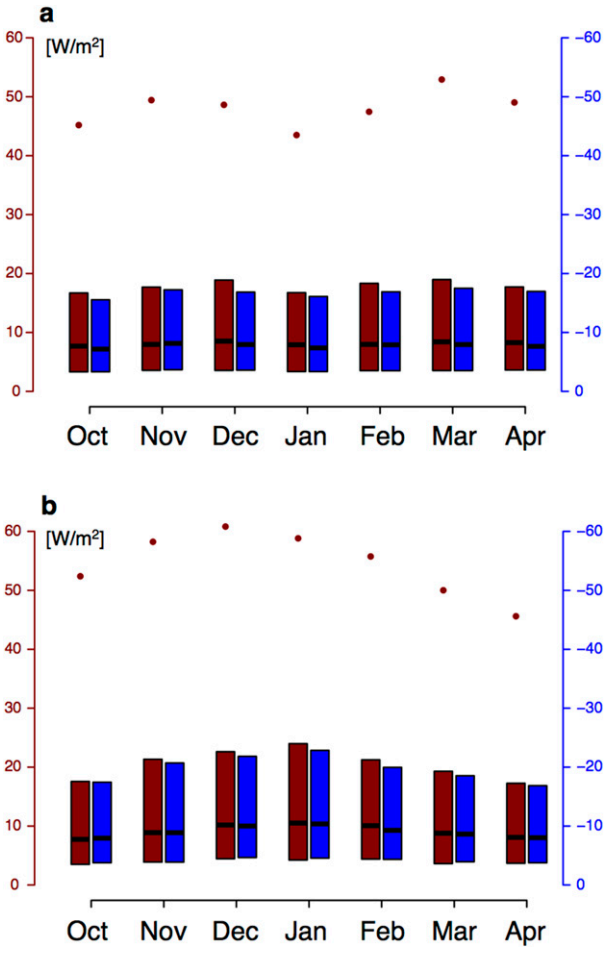

FIG. 7. Monthly distributions of Lagrangian EKE tendencies along cyclone tracks that propagate through (a) the central North Pacific and (b) North Atlantic. Lagrangian EKE tendencies are computed by differencing vertically integrated EKE along subsequent time steps in a life cycle; positive (red) and negative (blue) tendencies are treated individually. Each box spans the 25th–75th percentiles; the horizontal black lines in each box indicate the median. The red dots indicate the 90th percentile of the positive Lagrangian EKE tendency distributions. Target areas are shown in Fig. 1a. EKE is high-pass filtered (6-day cutoff).

d. Suppression of EKE, heat fluxes, and momentum fluxes at different levels

The midwinter suppression manifests itself mainly at upper levels, and less at lower levels (Fig. 8). In the North Pacific, EKE increases from July through October at 250 and 800 hPa (Figs. 8a,c). As midwinter approaches, the suppression of EKE is more pronounced with increasing altitude and is prolonged at 200 hPa (not shown). The evolutions of the meridional 800-hPa eddy heat and 320-K eddy PV fluxes are in line with the corresponding evolution of EKE, with some differences in early winter for the PV flux (Fig. 8). The latter is largely a consequence of the fact that the 250-hPa isobar (EKE) and the 320-K isentrope (PV flux) do not agree everywhere in altitude. North Pacific maximum mean EKE and heat flux at 800 hPa (Fig. 8c) occur during December, with no further increase during January and February before the decline during spring. The mean and median in the low-level heat flux and EKE evolution hence exhibit a midwinter plateau, while the upper percentiles exhibit a suppression (Fig. 8c).

EKE in the North Atlantic is not reduced during midwinter at 800 and 250 hPa compared to the shoulder

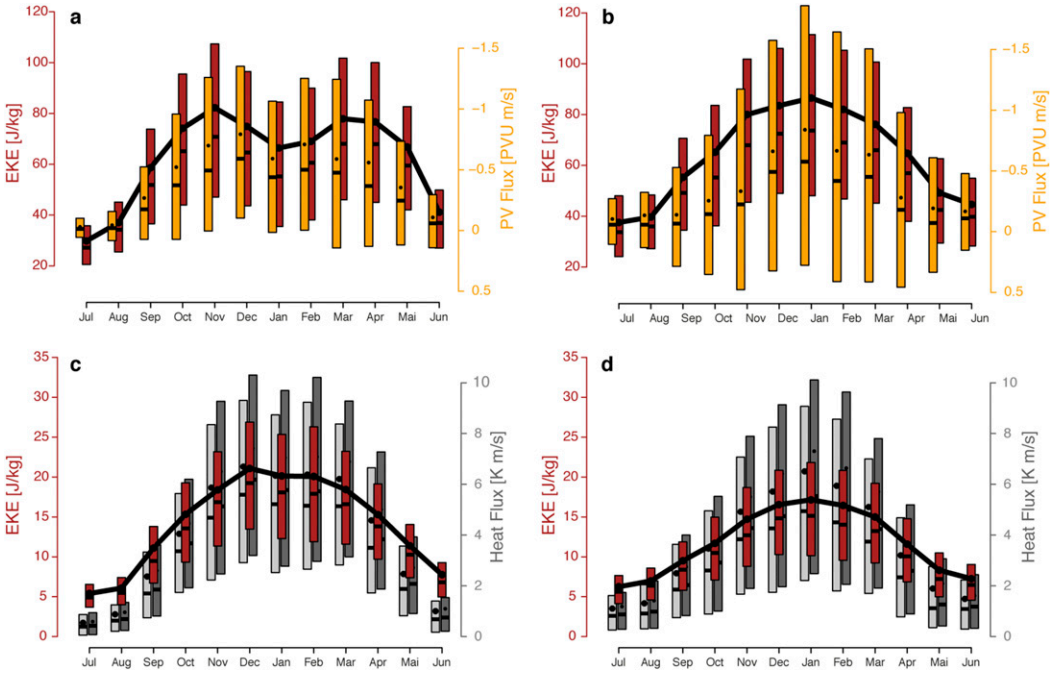

FIG. 8. Area-averaged distributions of 2–6-day bandpass-filtered (a),(b) 250-hPa EKE (red; J kg^{-1}) and 320-K meridional eddy PV flux [yellow; PVU m s^{-1} (1 PVU = 10^{-6} K kg^{-1} m^2 s^{-1})] and (c),(d) 800-hPa EKE (red; J kg^{-1}) and 800-hPa meridional eddy heat flux (light gray for temperature flux and dark gray for potential temperature flux; K m s^{-1}) in the (left) North Pacific (20°–60°N, 160°E–160°W) and (right) North Atlantic (20°–60°N, 30°–50°W). Each box spans the interquartile range, black dots indicate the mean, and black horizontal bars indicate the median value. The thick black lines connect the EKE mean values. Note the different scales for the axes at the different levels.

months (Figs. 8b,d). However, there is a plateau of EKE during December and January at 200 hPa (not shown). At 320 K, meridional eddy potential vorticity fluxes peak during January. At lower levels, eddy fluxes increase throughout the midwinter and acquire maxima during January, mirroring the behavior of EKE (Fig. 8d).

e. *Upstream fetch*

Another plausible hypothesis for the differences between the North Pacific and North Atlantic storm tracks in winter is that the storm tracks draw differently on moisture sources. It is possible that the North Pacific storm track draws moisture from the tropical warm pool region, leading to enhanced poleward moisture transport and ultimately enhanced net precipitation over the North Pacific relative to the North Atlantic (e.g., Warren 1983; Emile-Geay et al. 2003; Wills and Schneider 2015). The same enhanced net precipitation, and the release of latent heat associated with it, may stabilize the thermal stratification in the North Pacific relative to the North Atlantic, especially in winter when the moisture transport by transient eddies peaks (Peixoto and Oort 1992; Newman et al. 2012). This may generate a midwinter suppression of storm-track activity in the North Pacific relative to the North Atlantic. However, no sizable difference in source regions of air masses that constitute the lower troposphere in the central North Pacific is found, as seen by comparing a 5-day backward parcel trajectory density between October, January, and April (Fig. 9). The density highlights regions from which the North Pacific draws air. In particular, there is no clear enhanced transport from the tropical warm pool into the target area. Yet, the latent heat release over the North Pacific is still enhanced relative to the North Atlantic, and possibly affecting a wider area, leading to a greater upstream fetch for moisture transport in the North Pacific (Ferreira et al. 2010).

4. Eddy diffusivity

First, we briefly review some of the aspects related to the definition of an eddy diffusivity, before computing the observed eddy diffusivity based on a 30-yr parcel trajectory climatology.

a. *Theory*

The eddy diffusivity is proportional to the integral of the velocity autocorrelation of an air parcel (LaCasce

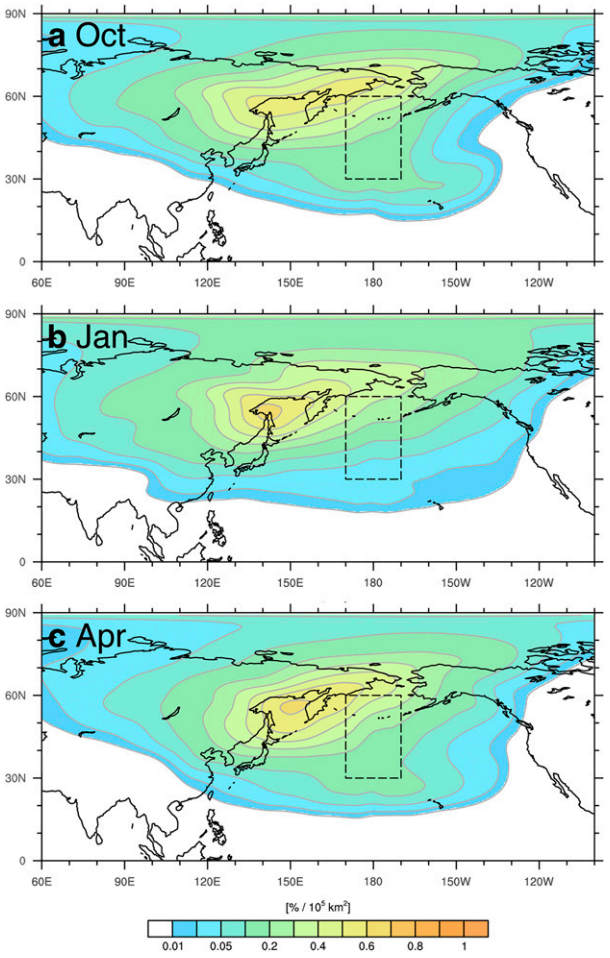

FIG. 9. Origin of air in the lower troposphere in the central Pacific (dashed boxes) during different months. Shown is the monthly mean probability density (shading) of air arriving within the next 5 days below 800 hPa in the target region. The probability density highlights regions from which the Pacific storm track draws air masses.

2008). Assuming a statistically stationary flow, that is, that the mean and the variance over a large number of particles is time-independent, Taylor (1922) derived the eddy diffusivity[3]

$$D(\mathbf{x}) = v_{\mathrm{rms}}^2 \int_0^t R(\mathbf{x}, \tau)\, d\tau, \tag{6}$$

where v_{rms} is a time-independent root-mean-square (RMS) velocity, $\mathbf{x} = (\lambda, \phi, p)$ is the particle position, τ is a given time period since particle release, and R is the Lagrangian velocity autocorrelation

$$R(\mathbf{x}, \tau) = \lim_{T\to\infty} \frac{1}{v_{\mathrm{rms}}^2 T} \int_0^T \tilde{v}(\mathbf{x}, t)\tilde{v}(\mathbf{x}, t+\tau)\, dt. \tag{7}$$

Here, and in what follows, we consider only the meridional parcel velocity component. In Eq. (7), $\tilde{v}(\mathbf{x}, t)$ denotes the meridional eddy velocity, that is, the fluctuation at time t around a characteristic mean velocity

$$\tilde{v}(\mathbf{x}, t) = v(\mathbf{x}, t) - \overline{v(\mathbf{x})}. \tag{8}$$

The mean velocity $\overline{v(\mathbf{x})}$ is computed by averaging the meridional parcel velocity over all parcel trajectory start times in our 30-yr climatology. The characteristic RMS velocity v_{rms} is then computed by averaging over all squared fluctuations around the mean velocity

$$v_{\mathrm{rms}}^2 = \frac{1}{n} \sum_n \tilde{v}^2, \tag{9}$$

where the subscript n runs over all released particle trajectories and trajectory times. In addition to this traditional method to estimate v_{rms}^2, we also use a 2–6-day bandpass filter in Eq. (8) to estimate v_{rms}^2 for a more direct comparison with the previously computed EKE and eddy fluxes (Fig. 8).

The sample Lagrangian autocorrelation [Eq. (7)] for our 30-yr trajectory climatology is, as in Swanson and Pierrehumbert (1997), computed from

$$R(\mathbf{x}, \tau) = \frac{\sum_n \left[\tilde{v}(\mathbf{x}_0, t_0)\tilde{v}(\mathbf{x}, t_0+\tau)\right]}{\sqrt{\sum_n \tilde{v}(\mathbf{x}_0, t_0)^2}\sqrt{\sum_n \tilde{v}(\mathbf{x}, t_0+\tau)^2}}, \tag{10}$$

where the subscript n runs over all trajectories, so the autocorrelation is computed across the trajectory sample. Initially the autcorrelation is unity. It approaches zero as the particle loses its "self correlation." In practice, the autocorrelation starts to oscillate around zero after the particle becomes decorrelated, indicating the importance of large-scale waves (Kao 1965; Kao and Bullock 1964).

b. *Lagrangian meridional autocorrelation and eddy diffusivity*

We first compute the Lagrangian autocorrelation R for the central North Pacific and the central North Atlantic based on the 30-yr trajectory climatology (Fig. 10). The autocorrelation curves share characteristics of a damped sinusoidal wave. In both basins, particle velocities decorrelate faster with increasing altitude, owing to more intense turbulence at higher levels. At the

[3] The diffusivity D can also be expressed as a time derivative of the second central moment (i.e., the mean dispersion $\overline{X}$): $D = 1/2(d/dt\overline{X}^2)$.

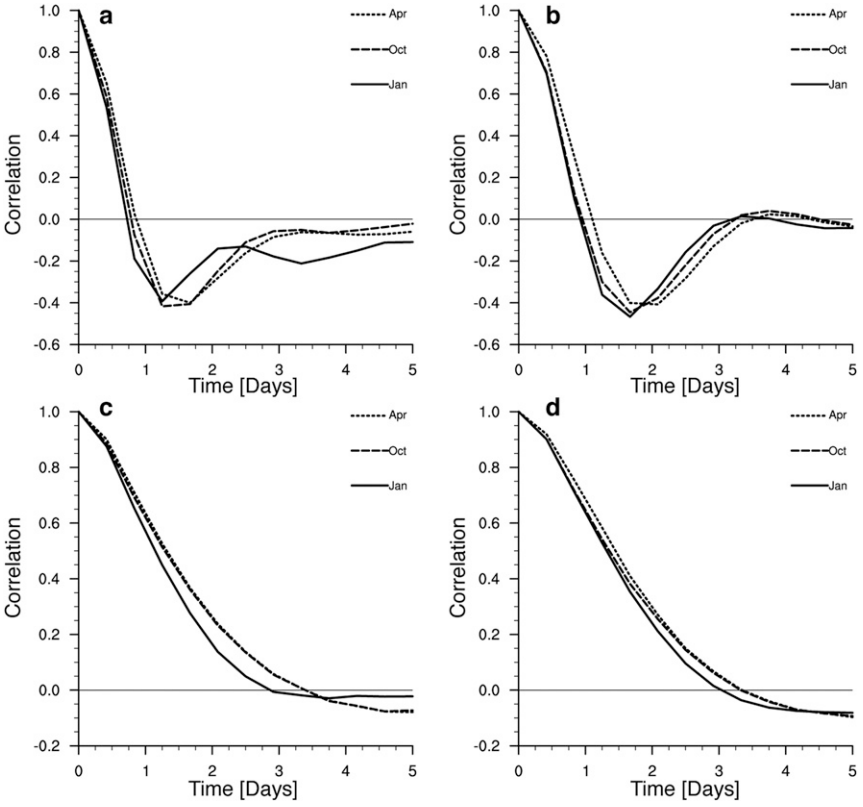

FIG. 10. Lagrangian meridional velocity autocorrelation based on 30 years of backward trajectories released at every grid point in the (left) central North Pacific (20°–60°N, 160°E–160°W) and (right) central North Atlantic (20°–60°N, 30°–50°W) at (a),(b) 200 and (c),(d) 800 hPa. The autocorrelation is shown for January (black solid line), October (dashed), and April (short dashed). Note the different scales in (a),(b) and (c),(d).

800-hPa level, R fluctuates near zero (Figs. 10c,d) after approximately 3 days, similar to what Swanson and Pierrehumbert (1997) found. Meridional particle velocities at 200 hPa become anticorrelated already after 0.5–1.0 days and fluctuate near zero after 1.5 days (Figs. 10a,b). In the North Pacific, the decorrelation also occurs more rapidly in midwinter at both levels (Figs. 10a,c). By contrast, the 800-hPa autocorrelation curves in the North Atlantic evolve less from October, through January, to April (Figs. 10b,d).

Next, the meridional parcel velocity variance v^2_{rms} is approximated from the 30-yr trajectory climatology from the four different vertical levels from which we released the trajectories. We note that our findings remain valid for all three examined vertical upper levels (300, 250, and 200 hPa). In the North Pacific, v^2_{rms} peaks in the upper troposphere during November and April and exhibits a clear midwinter minimum during January (Table 1). Lower levels do not exhibit a clear midwinter suppression in v^2_{rms}; instead, North Pacific v^2_{rms} peaks during December and January at 800 hPa (Table 1). However, the midwinter peak in baroclinicity (January) implies that there is a mild suppression or plateau (as already seen in the eddy heat flux in Fig. 8c).

In the North Atlantic, v^2_{rms} peaks during December at 250 hPa and declines through April afterward, which is in contrast to the North Pacific (Table 2). At 800 hPa in the North Atlantic, v^2_{rms} peaks during January (Table 2). Applying a bandpass filter to the meridional velocities from all parcel trajectories released from similar positions and months, the estimated v^2_{rms} is smaller by a factor of approximately 3–4 in the North Pacific and by a factor of 5–6 in the North Atlantic (Table 1 values in parentheses). The filtering does not strongly affect the overall seasonal evolution, with some exceptions, such as during November at 800 hPa in the North Pacific.

To obtain the eddy diffusivities, we first integrate R [Eq. (10)] over time. In theory, the autocorrelation tends to zero as time approaches infinity. However, the sample autocorrelation can sometimes get negative over time periods of several days because the integral depends strongly on the fluctuations around zero and the integration time period used in the

TABLE 1. Meridional velocity variance ($m^2 s^{-2}$) based on 30 years of 5-day backward trajectories released at every grid point in the central North Pacific (20°–60°N, 160°E–160°W) in 12-h intervals. The values in parentheses indicate the estimate based on a 2–6-day bandpass filter instead of the more traditional method of using squared deviations from the time-mean in the computation of the velocity variance [see Eq. (8)].

	North Pacific v^2_{rms}						
Level	Oct	Nov	Dec	Jan	Feb	Mar	Apr
250 hPa	146 (36.5)	147 (36.2)	138 (33.8)	129 (31.9)	131 (32.3)	139 (33.9)	139 (34.6)
800 hPa	46 (12.2)	57 (14.3)	59 (13.8)	59 (14.1)	56 (13.2)	56 (13.9)	52 (13.0)

trajectory computation (Fig. 10). We therefore estimate the integral using the trapezoidal rule until R approaches zero for the first time (Daoud et al. 2003). The results are listed in Tables 3 and 4. In the North Pacific at 250 hPa, the integral over R yields a Lagrangian decorrelation time of 6.7 h for December (Table 3). For October, we obtain 7.0 h, and 7.3 h for March. In the North Atlantic at 250 hPa, we obtain, for example, 7.8 h for December, 8.0 h for October, and 8.2 h for March (Table 4). Apparently, both basins exhibit reduced decorrelation times during midwinter. The reduced Lagrangian decorrelation times extend throughout the entire troposphere. These results suggest that the Lagrangian decorrelation time exhibits a minimum both in the upper and lower troposphere during December–January. This holds true in both basins and is broadly consistent with the reduction in eddy lifetimes (Fig. 3).

Next, from the velocity variance v^2_{rms} and the integrated autocorrelation we obtain the eddy diffusivities [Eq. (6)], shown in Fig. 11. Using the velocity variance obtained from bandpass-filtered parcel trajectory velocities in the North Pacific, the eddy diffusivity is lowest during midwinter at upper levels (Fig. 11a). At 800 hPa, eddy diffusivities in the North Pacific vary only little during winter (Fig. 11c). In the North Atlantic, by contrast, the eddy diffusivity peaks during winter at upper and at lower levels (Figs. 11b,c). From October to January, eddy diffusivity decreases in the North Pacific at 250 hPa by 15% ($133\,500\,m^2 s^{-1}$) (Fig. 11a). Of this reduction in eddy diffusivity, approximately 85% can be ascribed to changes in v^2_{rms} and 15% to changes in the Lagrangian decorrelation time. In the North Atlantic at 250 hPa, eddy diffusivity increases by 10% ($91\,000\,m^2 s^{-1}$) between November and January, and 95% of this increase can be ascribed to an increase in v^2_{rms}, and only 5% to changes in the Lagrangian decorrelation time.

Finally, the flux–gradient relationship allows us to estimate the eddy heat flux from the Lagrangian eddy diffusivities [Eq. (1)] and compare it to the observed values based on Eulerian statistics (Fig. 8). To this end, we compute the monthly mean area-averaged meridional temperature and PV gradients based on 6-hourly data (gray contour in Fig. 11) in both basins and multiply them by the eddy diffusivities obtained from the Lagrangian statistics (black contour in Fig. 11). The obtained ratio between the estimated and observed fluxes estimated from the flux–gradient relationship (Fig. 8) is shown near the bottom axis in Fig. 11. In the North Pacific, the PV flux overestimates the observed flux by a factor between 1.1 and 1.6, especially during the shoulder months (Fig. 11a). In the North Atlantic, the estimated PV flux overestimates the observed eddy PV flux by a factor up to 2.5 during the shoulder seasons, but it is close to the observed flux during midwinter. At 800 hPa, the estimated eddy heat flux is close to the observed flux throughout all months, with a minor tendency to underestimate the observed heat (temperature as well as potential temperature) flux by a factor of 0.7–0.9. The seasonal cycle is captured at both levels and in both basins. The differences between observed and estimated heat flux at lower levels likely is a consequence of nonconservative thermal processes. At upper levels, the disagreement likely is because the trajectory starting position at 250 hPa is not exactly collocated with the 320-K isentropic surface (which during winter on average is located between 250 and 300 hPa and between 30° and 60°N). This disagreement between isobaric and isentropic surfaces is larger

TABLE 2. Meridional velocity variance ($m^2 s^{-2}$) based on 30 years of 5-day backward trajectories released at every grid point in the central North Atlantic (20°–60°N, 30°–50°W) in 12-h intervals. Parenthetical values are analogous to Table 1.

	North Atlantic v^2_{rms}						
Level	Oct	Nov	Dec	Jan	Feb	Mar	Apr
250 hPa	212 (31.7)	238 (35.7)	256 (37.9)	252 (37.4)	242 (35.6)	234 (35.6)	219 (32.8)
800 hPa	48 (7.3)	61 (9.3)	69 (10.8)	72 (11.0)	69 (10.4)	66 (10.1)	57 (8.5)

TABLE 3. Lagrangian decorrelation time (h) based on 30 years of 5-day backward trajectories released at every grid point in the central North Pacific (20°–60°N, 160°E–160°W) in 12-h intervals. The standard deviation for the individual months is given in parentheses.

	Lagrangian decorrelation (North Pacific)						
Level	Oct	Nov	Dec	Jan	Feb	Mar	Apr
250 hPa	7.0 (0.4)	6.9 (0.5)	6.7 (0.5)	6.8 (0.7)	7.1 (0.7)	7.3 (0.6)	7.6 (0.4)
800 hPa	20.1 (2.1)	18.5 (1.9)	17.2 (1.3)	17.7 (1.7)	18.3 (1.8)	18.7 (1.6)	20.4 (1.5)

during the shoulder months, where the error in our estimation is also largest. However, the suppression in the meridional velocity variance clearly translates directly into a reduction in the meridional eddy PV flux via reduction in eddy diffusivity. The precise reduction in eddy diffusivity is due to a combination of changes in velocity variance and Lagrangian decorrelation times, with the velocity variance dominating.

5. Summary

We compiled a comprehensive phenomenology of winter storm-track variability from Eulerian and Lagrangian perspectives, which we summarize as follows. In the North Pacific, the number of surface cyclones is highest during midwinter, but the mean EKE per cyclone life cycle is reduced relative to the shoulder months. Hence, the midwinter reduction in upper-level eddy activity (e.g., Penny et al. 2010) is not associated with a reduction in the number of surface cyclones. In the North Atlantic, by contrast, the mean EKE per cyclone life cycle is highest in early winter, as is the cyclone number.

Lagrangian analyses of cyclone tracks revealed that the eddy lifetime near the surface is lowest in the North Pacific in midwinter, with a weaker reduction in the North Atlantic. This finding is consistent with an increased group velocity of upper-level eddies (e.g., Chang 2001). Additionally, Lagrangian EKE tendencies are suppressed in the North Pacific in midwinter, but not in the North Atlantic.

The area of peak baroclinic conversion rates retreats during midwinter in the North Pacific to a smaller area over the Kuroshio Extension. In contrast, in the North Atlantic, baroclinic conversion peaks during January over the Gulf Stream region. In both basins, maximum baroclinic EKE conversion occurs upstream of the local EKE maximum, as seen in previous studies (e.g., Chang 2001). Barotropic conversion, though smaller compared to baroclinic conversion, is equally affected by the midwinter suppression. The midwinter suppression in meridional eddy potential vorticity fluxes and EKE is pronounced at upper-tropospheric levels in the North Pacific. In the lower troposphere, meridional heat fluxes and EKE exhibit a midwinter plateau rather than a minimum. Because baroclinic conversion is expected to scale with the eddy fluxes, it is unclear if the baroclinic midwinter suppression is a cause or a consequence of the suppression in eddy fluxes and EKE. Over the North Atlantic, the lower-tropospheric eddy heat flux closely follows the seasonal cycle of baroclinicity, and the upper-tropospheric eddy potential vorticity flux follows that of the mean meridional potential vorticity gradient.

Finally, we computed a climatology of the Lagrangian eddy diffusivity in the North Pacific and North Atlantic based on 30 years of parcel trajectories. The results indicate a midwinter reduction in the eddy diffusivity, which is most pronounced at upper levels in the North Pacific, where both the Lagrangian decorrelation time and the RMS velocity have midwinter minima. The midwinter reduction in eddy diffusivities is most pronounced in the North Pacific, while in the North Atlantic eddy diffusivities exhibit a midwinter maximum. The Lagrangian eddy diffusivities multiplied by the mean potential vorticity gradients slightly overestimate the midwinter eddy potential vorticity flux obtained from synoptic-scale bandpass-filtered data. For the lower-tropospheric heat flux, the estimated eddy diffusivity slightly underestimates the observed eddy heat flux. The difference between observed and estimated heat fluxes likely results from nonconservative thermal processes; the difference between the PV fluxes likely results from the different heights of the analyzed isentropic (observed PV flux) and isobaric surfaces (estimated eddy diffusivity).

The seasonal cycle of eddy diffusivities in both basins can be traced partly to a midwinter reduction in the Lagrangian decorrelation time, consistent with the reduction in eddy lifetimes. However, the seasonal cycle in the North Pacific is dominated by the reduction in the RMS velocity,

TABLE 4. Lagrangian decorrelation time (h) based on 30 years of 5-day backward trajectories released at every grid point in the central North Atlantic (20°–60°N, 30°–50°W) in 12-h intervals.

	Lagrangian decorrelation (North Atlantic)						
Level	Oct	Nov	Dec	Jan	Feb	Mar	Apr
250 hPa	8.0	7.8	7.8	8.1	8.2	8.2	8.4
800 hPa	21.9	21.4	20.7	20.9	21.4	21.3	22.5

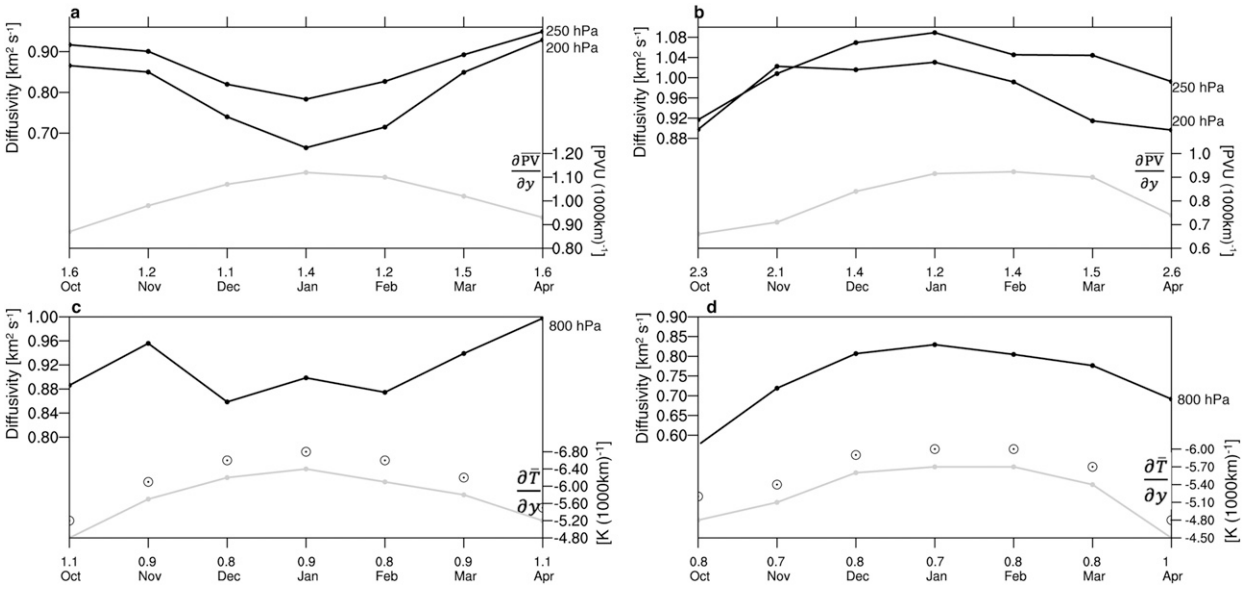

FIG. 11. Eddy diffusivities (black lines; $km^2 s^{-1}$) at (a),(b) 200 and 250 hPa and (c),(d) 800 hPa based on 30 years of backward parcel trajectories released in the (left) central North Pacific (20°–60°N, 160°E–160°W) and (right) central North Atlantic (20°–60°N, 30°–50°W). Gray lines indicate the area-averaged mean meridional 320-K PV gradient [PVU $(10^3 km)^{-1}$] in (a),(b) and the 800-hPa temperature gradient [K $(10^3 km)^{-1}$] in (c),(d). Circles with center dots in (c),(d) indicate meridional 800-hPa potential temperature gradient. The numbers above each month indicate the fraction between the estimated and the observed PV in (a),(b) and heat fluxes in (c),(d) (observed values are shown in Fig. 8).

consistent with the reduction in EKE; in the North Atlantic, a milder reduction in Lagrangian decorrelation time is offset by a maximum in the RMS velocity. Consequently, the midwinter suppression in velocity variance in the North Pacific can translate into a reduction in upper-level eddy potential vorticity and lower-level eddy heat fluxes via a reduction in eddy diffusivities. However, the exact suppression in eddy heat and potential vorticity fluxes depends on a combination of changes in both velocity variance and Lagrangian decorrelation time.

What emerges is a consistent picture of how various quantities related to eddy properties are interrelated. The picture does not, however, point to a clear dynamical cause of the midwinter suppression over the North Pacific. Our findings buttress the importance of processes internal to storm-track dynamics for the midwinter suppression; they argue against a dominant role of upstream seeding effects for the midwinter suppression. Attempts at dynamical explanations may thus focus on causes of the midwinter reduction in Lagrangian decorrelation time (or eddy lifetime) and in parcel velocity variance over the North Pacific, for example, during different jet regimes.

Acknowledgments. Sebastian Schemm acknowledges funding from the Swiss National Science Foundation (Grants P300P2_167745 and P3P3P2_167747). ECMWF is acknowledged for providing the ERA-Interim dataset. We are grateful to Farid Ait-Chaalal for helpful comments during the course of the analysis. We also thank three anonymous reviewers and Hisashi Nakamura for their helpful comments during the review process.

REFERENCES

Ambaum, M. H. P., and L. Novak, 2014: A nonlinear oscillator describing storm track variability. *Quart. J. Roy. Meteor. Soc.*, **140**, 2680–2684, https://doi.org/10.1002/qj.2352.

Baehr, C., B. Pouponneau, F. Ayrault, and A. Joly, 1999: Dynamical characterization of the FASTEX cyclogenesis cases. *Quart. J. Roy. Meteor. Soc.*, **125**, 3469–3494, https://doi.org/10.1002/qj.49712556117.

Bengtsson, L., K. I. Hodges, and E. Roeckner, 2006: Storm tracks and climate change. *J. Climate*, **19**, 3518–3543, https://doi.org/10.1175/JCLI3815.1.

Chang, E. K. M., 2001: GCM and observational diagnoses of the seasonal and interannual variations of the Pacific storm track during the cool season. *J. Atmos. Sci.*, **58**, 1784–1800, https://doi.org/10.1175/1520-0469(2001)058<1784:GAODOT>2.0.CO;2.

——, and S. Song, 2006: The seasonal cycles in the distribution of precipitation around cyclones in the western North Pacific and Atlantic. *J. Atmos. Sci.*, **63**, 815–839, https://doi.org/10.1175/JAS3661.1.

——, and P. Zurita-Gotor, 2007: Simulating the seasonal cycle of the Northern Hemisphere storm tracks using idealized nonlinear storm-track models. *J. Atmos. Sci.*, **64**, 2309–2331, https://doi.org/10.1175/JAS3957.1.

——, and Y. Guo, 2011: Comments on "The source of the midwinter suppression in storminess over the North Pacific." *J. Climate*, **24**, 5187–5191, https://doi.org/10.1175/2011JCLI3987.1.

——, and ——, 2012: Is Pacific storm-track activity correlated with the strength of upstream wave seeding? *J. Climate*, **25**, 5768–5776, https://doi.org/10.1175/JCLI-D-11-00555.1.

——, S. Lee, and K. L. Swanson, 2002: Storm track dynamics. *J. Climate*, **15**, 2163–2183, https://doi.org/10.1175/1520-0442(2002)015<02163:STD>2.0.CO;2.

Charney, J. G., 1947: The dynamics of long waves in a baroclinic westerly current. *J. Meteor.*, **4**, 136–162, https://doi.org/10.1175/1520-0469(1947)004<0136:TDOLWI>2.0.CO;2.

Coronel, B., D. Ricard, G. Rivière, and P. Arbogast, 2015: Role of moist processes in the tracks of idealized midlatitude surface cyclones. *J. Atmos. Sci.*, **72**, 2979–2996, https://doi.org/10.1175/JAS-D-14-0337.1.

Daoud, W. Z., J. D. W. Kahl, and J. K. Ghorai, 2003: On the synoptic-scale Lagrangian autocorrelation function. *J. Appl. Meteor.*, **42**, 318–324, https://doi.org/10.1175/1520-0450(2003)042<0318:OTSSLA>2.0.CO;2.

Dee, D. P., and Coauthors, 2011: The ERA-Interim reanalysis: Configuration and performance of the data assimilation system. *Quart. J. Roy. Meteor. Soc.*, **137**, 553–597, https://doi.org/10.1002/qj.828.

Deng, Y., and M. Mak, 2005: An idealized model study relevant to the dynamics of the midwinter minimum of the Pacific storm track. *J. Atmos. Sci.*, **62**, 1209–1225, https://doi.org/10.1175/JAS3400.1.

Eady, E. T., 1949: Long waves and cyclone waves. *Tellus*, **1** (3), 33–52, https://doi.org/10.3402/tellusa.v1i3.8507.

Emile-Geay, J., M. A. Cane, N. Naik, R. Seager, A. C. Clement, and A. van Geen, 2003: Warren revisited: Atmospheric freshwater fluxes and "Why is no deep water formed in the North Pacific." *J. Geophys. Res.*, **108**, 3178, https://doi.org/10.1029/2001JC001058.

Ferreira, D., J. Marshall, and J.-M. Campin, 2010: Localization of deep water formation: Role of atmospheric moisture transport and geometrical constraints on ocean circulation. *J. Climate*, **23**, 1456–1476, https://doi.org/10.1175/2009JCLI3197.1.

Fyfe, J. C., 2003: Extratropical Southern Hemisphere cyclones: Harbingers of climate change? *J. Climate*, **16**, 2802–2805, https://doi.org/10.1175/1520-0442(2003)016<2802:ESHCHO>2.0.CO;2.

Harnik, N., and E. K. Chang, 2004: The effects of variations in jet width on the growth of baroclinic waves: Implications for midwinter Pacific storm track variability. *J. Atmos. Sci.*, **61**, 23–40, https://doi.org/10.1175/1520-0469(2004)061<0023:TEOVIJ>2.0.CO;2.

Harvey, B. J., L. C. Shaffrey, and T. J. Woollings, 2014: Equator-to-pole temperature differences and the extra-tropical storm track responses of the CMIP5 climate models. *Climate Dyn.*, **43**, 1171–1182, https://doi.org/10.1007/s00382-013-1883-9.

Hoskins, B. J., and K. I. Hodges, 2002: New perspectives on the Northern Hemisphere winter storm tracks. *J. Atmos. Sci.*, **59**, 1041–1061, https://doi.org/10.1175/1520-0469(2002)059<1041:NPOTNH>2.0.CO;2.

——, and ——, 2005: A new perspective on Southern Hemisphere storm tracks. *J. Climate*, **18**, 4108–4129, https://doi.org/10.1175/JCLI3570.1.

Kao, S., 1965: Some aspects of the large-scale turbulence and diffusion in the atmosphere. *Quart. J. Roy. Meteor. Soc.*, **91**, 10–17, https://doi.org/10.1002/qj.49709138703.

——, and W. S. Bullock, 1964: Lagrangian and Eulerian correlations and energy spectra of geostrophic velocities. *Quart. J. Roy. Meteor. Soc.*, **90**, 166–174, https://doi.org/10.1002/qj.49709038406.

Keyser, D., and M. A. Shapiro, 1986: A review of the structure and dynamics of upper-level frontal zones. *Mon. Wea. Rev.*, **114**, 452–499, https://doi.org/10.1175/1520-0493(1986)114<0452:AROTSA>2.0.CO;2.

LaCasce, J. H., 2008: Statistics from Lagrangian observations. *Prog. Oceanogr.*, **77**, 1–29, https://doi.org/10.1016/j.pocean.2008.02.002.

Lee, S., 2000: Barotropic effects on atmospheric storm tracks. *J. Atmos. Sci.*, **57**, 1420–1435, https://doi.org/10.1175/1520-0469(2000)057<1420:BEOAST>2.0.CO;2.

Lindzen, R. S., and B. Farrell, 1980: A simple approximate result for the maximum growth rate of baroclinic instabilities. *J. Atmos. Sci.*, **37**, 1648–1654, https://doi.org/10.1175/1520-0469(1980)037<1648:ASARFT>2.0.CO;2.

Nakamura, H., 1992: Midwinter suppression of baroclinic wave activity in the Pacific. *J. Atmos. Sci.*, **49**, 1629–1642, https://doi.org/10.1175/1520-0469(1992)049<1629:MSOBWA>2.0.CO;2.

——, and T. Sampe, 2002: Trapping of synoptic-scale disturbances into the North-Pacific subtropical jet core in midwinter. *Geophys. Res. Lett.*, **29**, 8-1–8-4, https://doi.org/10.1029/2002GL015535.

——, and A. Shimpo, 2004: Seasonal variations in the Southern Hemisphere storm tracks and jet streams as revealed in a reanalysis dataset. *J. Climate*, **17**, 1828–1844, https://doi.org/10.1175/1520-0442(2004)017<1828:SVITSH>2.0.CO;2.

Neu, U., and Coauthors, 2013: IMILAST: A community effort to intercompare extratropical cyclone detection and tracking algorithms. *Bull. Amer. Meteor. Soc.*, **94**, 529–547, https://doi.org/10.1175/BAMS-D-11-00154.1.

Newman, M., G. N. Kiladis, K. M. Weickmann, F. M. Ralph, and P. D. Sardeshmukh, 2012: Relative contributions of synoptic and low-frequency eddies to time-mean atmospheric moisture transport, including the role of atmospheric rivers. *J. Climate*, **25**, 7341–7361, https://doi.org/10.1175/JCLI-D-11-00665.1.

O'Gorman, P. A., 2010: Understanding the varied response of the extratropical storm tracks to climate change. *Proc. Natl. Acad. Sci. USA*, **107**, 19 176–19 180, https://doi.org/10.1073/pnas.1011547107.

——, and T. Schneider, 2008: Energy of midlatitude transient eddies in idealized simulations of changed climates. *J. Climate*, **21**, 5797–5806, https://doi.org/10.1175/2008JCLI2099.1.

Orlanski, I., and J. Katzfey, 1991: The life cycle of a cyclone wave in the Southern Hemisphere. Part I: Eddy energy budget. *J. Atmos. Sci.*, **48**, 1972–1998, https://doi.org/10.1175/1520-0469(1991)048<1972:TLCOAC>2.0.CO;2.

——, and J. P. Sheldon, 1995: Stages in the energetics of baroclinic systems. *Tellus*, **47A**, 605–628, https://doi.org/10.3402/tellusa.v47i5.11553.

Park, H., J. C. Chiang, and S. Son, 2010: The role of the central Asian mountains on the midwinter suppression of North Pacific storminess. *J. Atmos. Sci.*, **67**, 3706–3720, https://doi.org/10.1175/2010JAS3349.1.

Peixoto, J. P., and A. H. Oort, 1992: *Physics of Climate.* American Institute of Physics, 520 pp.

Penny, S., G. H. Roe, and D. S. Battisti, 2010: The source of the midwinter suppression in storminess over the North Pacific. *J. Climate*, **23**, 634–648, https://doi.org/10.1175/2009JCLI2904.1.

——, ——, and ——, 2011: Reply. *J. Climate*, **24**, 5192–5194, https://doi.org/10.1175/2011JCLI4187.1.

Rivière, G., P. Arbogast, and A. Joly, 2015: Eddy kinetic energy redistribution within windstorms Klaus and Friedhelm. *Quart. J. Roy. Meteor. Soc.*, **141**, 925–938, https://doi.org/10.1002/qj.2412.

Schemm, S., L. M. Ciasto, C. Li, and N. G. Kvamstø, 2016: Influence of tropical Pacific sea surface temperature on the genesis of Gulf Stream cyclones. *J. Atmos. Sci.*, **73**, 4203–4214, https://doi.org/10.1175/JAS-D-16-0072.1.

Schneider, T., and C. C. Walker, 2008: Scaling laws and regime transitions of macroturbulence in dry atmospheres. *J. Atmos. Sci.*, **65**, 2153–2173, https://doi.org/10.1175/2007JAS2616.1.

——, P. A. O'Gorman, and X. J. Levine, 2010: Water vapor and the dynamics of climate changes. *Rev. Geophys.*, **48**, RG3001, https://doi.org/10.1029/2009RG000302.

Shaw, T. A., and Coauthors, 2016: Storm track processes and the opposing influences of climate change. *Nat. Geosci.*, **9**, 656–664, https://doi.org/10.1038/ngeo2783.

Sprenger, M., and H. Wernli, 2015: The LAGRANTO Lagrangian analysis tool—Version 2.0. *Geosci. Model Dev.*, **8**, 2569–2586, https://doi.org/10.5194/gmd-8-2569-2015.

——, and Coauthors, 2017: Global climatologies of Eulerian and Lagrangian flow features based on ERA-Interim. *Bull. Amer. Meteor. Soc.*, **98**, 1739–1784, https://doi.org/10.1175/BAMS-D-15-00299.1.

Stone, P. H., and D. A. Miller, 1980: Empirical relations between seasonal changes in meridional temperature gradients and meridional fluxes of heat. *J. Atmos. Sci.*, **37**, 1708–1721, https://doi.org/10.1175/1520-0469(1980)037<1708:ERBSCI>2.0.CO;2.

Swanson, K. L., and R. T. Pierrehumbert, 1997: Lower-tropospheric heat transport in the Pacific storm track. *J. Atmos. Sci.*, **54**, 1533–1543, https://doi.org/10.1175/1520-0469(1997)054<1533:LTHTIT>2.0.CO;2.

Taylor, G. I., 1922: Diffusion by continuous movements. *Proc. London Math. Soc.*, **20**, 196–212, https://doi.org/10.1112/plms/s2-20.1.196.

Thompson, D. W. J., and T. Birner, 2012: On the linkages between the tropospheric isentropic slope and eddy fluxes of heat during Northern Hemisphere winter. *J. Atmos. Sci.*, **69**, 1811–1823, https://doi.org/10.1175/JAS-D-11-0187.1.

——, and E. A. Barnes, 2014: Periodic variability in the large-scale Southern Hemisphere atmospheric circulation. *Science*, **343**, 641–645, https://doi.org/10.1126/science.1247660.

Trenberth, K. E., 1991: Storm tracks in the Southern Hemisphere. *J. Atmos. Sci.*, **48**, 2159–2178, https://doi.org/10.1175/1520-0469(1991)048<2159:STITSH>2.0.CO;2.

Uccellini, L. W., 1990: Processes contributing to the rapid development of extratropical cyclones. *Extratropical Cyclones, The Erik Palmén Memorial Volume*, C. W. Newton and E. O. Holopainen, Eds., Amer. Meteor. Soc., 81–105.

Wallace, J. M., G.-H. Lim, and M. L. Blackmon, 1988: Relationship between cyclone tracks, anticyclone tracks and baroclinic waveguides. *J. Atmos. Sci.*, **45**, 439–462, https://doi.org/10.1175/1520-0469(1988)045<0439:RBCTAT>2.0.CO;2.

Warren, B. A., 1983: Why is no deep water formed in the North Pacific? *J. Mar. Res.*, **41**, 327–347, https://doi.org/10.1357/002224083788520207.

Wernli, H., and H. C. Davies, 1997: A Lagrangian-based analysis of extratropical cyclones. I: The method and some applications. *Quart. J. Roy. Meteor. Soc.*, **123**, 467–489, https://doi.org/10.1002/qj.49712353811.

——, and C. Schwierz, 2006: Surface cyclones in the ERA-40 dataset (1958–2001). Part I: Novel identification method and global climatology. *J. Atmos. Sci.*, **63**, 2486–2507, https://doi.org/10.1175/JAS3766.1.

Wills, R. C., and T. Schneider, 2015: Stationary eddies and the zonal asymmetry of net precipitation and ocean freshwater forcing. *J. Climate*, **28**, 5115–5133, https://doi.org/10.1175/JCLI-D-14-00573.1.

Yin, J. H., 2005: A consistent poleward shift of the storm tracks in simulations of 21st century climate. *Geophys. Res. Lett.*, **32**, L18701, https://doi.org/10.1029/2005GL023684.